Dynamic Bone Imaging with ^{99m}Tc-Labeled Diphosphonates and ^{18}F-NaF: Mechanisms and Applications

Ka Kit Wong[1,2] and Morand Piert[1]

[1]*Nuclear Medicine/Radiology Department, University of Michigan Hospital, Ann Arbor, Michigan; and* [2]*Nuclear Medicine Service, Department of Veterans Affairs Health System, Ann Arbor, Michigan*

Learning Objectives: On successful completion of this activity, participants should be able to (1) appreciate the physiologic mechanisms underlying uptake of bone-seeking radiopharmaceuticals used to assess bone perfusion and turnover and note the differences between ^{18}F-NaF and ^{99m}Tc-labeled diphosphonates; (2) discuss the use of bone scintigraphy for evaluation of bone viability and metabolic bone disorders and appreciate the potential role of quantitative dynamic ^{18}F-NaF PET for evaluation of response to therapy; and (3) discuss indications for ^{99m}Tc-labeled diphosphonate bone scans and ^{18}F-NaF PET/CT for oncologic staging and appreciate quantitative methods on static and dynamic bone imaging as imaging biomarkers of treatment response using novel systemic therapies for metastatic castrate-resistant prostate cancer as a model.

Financial Disclosure: The authors of this article have indicated no relevant relationships that could be perceived as a real or apparent conflict of interest.

CME Credit: SNMMI is accredited by the Accreditation Council for Continuing Medical Education (ACCME) to sponsor continuing education for physicians. SNMMI designates each *JNM* continuing education article for a maximum of 2.0 AMA PRA Category 1 Credits. Physicians should claim only credit commensurate with the extent of their participation in the activity. For CE credit, participants can access this activity through the SNMMI Web site (http://www.snmmi.org/ce_online) through April 2016.

Dynamic bone scanning with ^{99m}Tc-labeled diphosphonates and ^{18}F-labeled sodium fluoride provides functional information sensitive for subtle changes in bone turnover and perfusion, which assists the clinical management of numerous osseous pathologies. This article reviews the mechanisms of uptake of ^{99m}Tc-labeled diphosphonates and ^{18}F-sodium fluoride and discusses and compares the performance of these bone-seeking radiotracers for clinical and research applications, using dynamic and multiple-time-point imaging protocols and quantitative techniques.

Key Words: ^{99m}Tc-methyl-diphosphonate; ^{18}F-NaF; dynamic imaging

J Nucl Med 2013; 54:590–599
DOI: 10.2967/jnumed.112.114298

Sodium fluoride labeled with ^{18}F (^{18}F-NaF) for bone scanning was introduced in 1962 by Blau et al. (*1*) and subsequently was approved for clinical use by the U.S. Food and Drug Administration in 1972. At the time, images were acquired with rectilinear scanners equipped with thick NaI(Tl) crystals. After the introduction and widespread acceptance of new thin-crystal γ-cameras optimized for imaging with ^{99m}Tc, the introduction of ^{99m}Tc-labeled diphosphonates (^{99m}Tc-methyl diphosphonate [^{99m}Tc-MDP] and ^{99m}Tc-hydroxymethylene diphosphonate) replaced ^{18}F-NaF bone scans in the mid 1970s.

The widespread availability of PET and PET/CT cameras in the United States has led to renewed interest in ^{18}F-NaF bone scanning, with ^{18}F-NaF PET first described in 1993 for clinical use (*2*). It provides highly sensitive, 3-dimensional imaging of the skeleton, with demonstrable utility in a growing range of benign and malignant bone disorders. ^{18}F-NaF PET has the advantages of high spatial resolution, attenuation correction, 3-dimensional tomographic images, and hybrid PET/CT imaging (*3–5*). ^{18}F-NaF PET is amenable to kinetic modeling, in particular quantitative assessment of bone perfusion and bone turnover, readily derived from dynamic PET acquisition, typically over 60 min (*3–5*). Recent guidelines have been published by the Society of Nuclear Medicine and Molecular Imaging for ^{18}F-NaF PET and PET/CT (*6*).

UPTAKE MECHANISMS OF BONE-SEEKING RADIOPHARMACEUTICALS

Bone is a composite material of inorganic crystals bound to protein. The mineral phase, built of crystals containing mainly calcium and phosphate, is called hydroxyapatite. This mineral phase is bound to a matrix largely consisting of a single protein, collagen. The mineral content determines the stiffness of bone. Without sufficient mineralization, bones will plastically deform under load. Collagen provides toughness to bone, making it less brittle so that it better resists mechanical stress. The healthy adult bone is in homeostasis, with a constant rate of remodeling due to the activity of osteoblasts laying down new bone and osteoclasts resorbing old bone. Bone adapts to repetitive mechanical stresses largely by changing its size and shape, which are major determinants of its resistance to fracture (*7*).

Received Jan. 23, 2013; revision accepted Feb. 28, 2013.
For correspondence or reprints contact: Morand Piert, University of Michigan Health System, Division of Nuclear Medicine, Department of Radiology, University Hospital B1G505C, 1500 E. Medical Center Dr., Ann Arbor, MI 48109-0028.
E-mail: mpiert@med.umich.edu
Published online Mar. 12, 2013.

Anatomically, bone tissue consists of compact (cortical) and cancellous (trabecular) bone, which perform different functions; compact bone forms the diaphyses of long bones and the surface of flat bones, whereas cancellous bone is found in the epiphyseal and metaphyseal regions of long bones and the interior of flat bones. Bone is in a constant state of remodeling or turnover, which is essentially a surface phenomenon. Although cortical bone forms most of the bone mass, it represents the minority of bone surface. By comparison, cancellous bone forms only 20% of the bone mass but accounts for 80% of the bone turnover associated with remodeling (*8*).

Physiologic Mechanism of Radiopharmaceutical Uptake

The pharmacokinetics of bone-seeking radiotracers essentially depend on the rates of bone uptake and elimination from the circulation via renal excretion.

Radiotracer Delivery

^{99m}Tc-labeled diphosphonates (^{99m}Tc-MDP and ^{99m}Tc-hydroxymethylenediphosphonate) and ^{18}F-NaF are essentially markers of both bone perfusion and bone turnover (*9*). After intravenous administration, the principal uptake mechanism of bone-seeking radiotracers involves adsorption onto or into the crystalline structure of hydroxyapatite. The first step in this cascade is radiotracer delivery, which depends on local blood flow and the rate of radiotracer extraction by bone. ^{99m}Tc-MDP undergoes protein binding in blood, which increases over time from around 25% at injection to about 50% at 4 h after injection (*10*). Only unbound tracer will be available for bone uptake. Although ^{18}F-NaF kinetics are not affected by protein binding, ^{18}F-NaF is transported by red blood cells with an erythrocyte concentration of roughly half that in plasma. As a result, ^{18}F-NaF concentrations are about 10%–25% higher in plasma than in whole blood (*11*).

According to the simplified Renkin and Crone capillary transport model (*12*), the net exchange of a substance between blood and tissue depends on blood flow, surface area, and the permeability of the capillary system. ^{99m}Tc-MDP undergoes passive diffusion through the capillary wall into the extravascular space (*13*). The diffusion rate is proportional to the molecular size; therefore, diffusion of small molecules is expected to be more rapid than that of ^{99m}Tc-diphosphonates (*14*). In addition, there is evidence that the extraction fraction of ^{99m}Tc-diphosphonates varies with blood flow. Performing outflow dilution experiments in the tibia of dogs, McCarthy et al. showed that the extraction fraction of ^{99m}Tc-MDP decreased substantially with increasing blood flow (*15*). In addition, they determined that the permeability-surface area remained unchanged, indicating that additional recruitment of capillaries under high-flow conditions does not occur. Figure 1 demonstrates the effect of increased blood flow on ^{99m}Tc-MDP uptake to the entire lower extremity secondary to the presence of a primary bone malignancy.

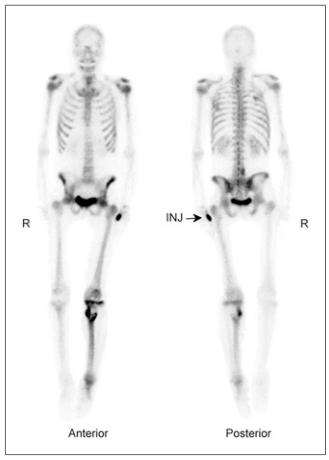

FIGURE 1. Diffusely increased ^{99m}Tc-MDP uptake of left lower extremity on delayed-phase whole-body bone scan (anterior and posterior projections) as result of increased blood flow due to osteosarcoma in proximal tibia. INJ = injection site.

In contrast to γ-camera imaging, PET imaging allows absolute quantification of radiotracer concentrations in tissue. Dynamic PET compartment modeling is needed to measure bone blood flow and the metabolic rate of fluoride binding to bone. Using this technique, we previously measured bone blood flow and extraction fraction of ^{18}F-NaF noninvasively, comparing the uptake of ^{15}O-H_2O and ^{18}F-NaF in vertebral bodies of mini pigs (*11*). The mean vertebral blood flow (K_1) as measured by ^{15}O-H_2O was 0.145 ± 0.047 mL/(min·cm^3) using a 1-tissue-compartment model. Under isometric low-intensity exercise, bone blood flow increases 2.3-fold in humans (*16*). At typical flow rates in bone, ^{15}O-H_2O is a freely diffusible tracer; thus, its extraction into tissue approaches 100% in a single capillary passage (*17*). Since K_1 is the product of blood flow and the extraction fraction, the quotient of corresponding ^{15}O-H_2O and K_1 values is an estimate for the regional extraction fraction of ^{18}F-NaF. Our results indicated that the extraction fraction of ^{18}F-NaF decreased from about 100% at low-flow conditions to approximately 40% at high flow (*11*). Correcting K_1 on the basis of extraction fraction estimates allows bone blood flow measurement with dynamic ^{18}F-NaF PET (*18*). Since measurements of the extraction fraction for ^{18}F-NaF and ^{99m}Tc-diphosphonates have been performed using different techniques, their results cannot be directly compared. However, it appears that the extraction fraction of ^{99m}Tc-diphosphonates is indeed substantially smaller than that of ^{18}F-NaF.

Radiotracer Localization to Bone

The mechanism of binding of extravascular ^{99m}Tc-diphosphonates to bone is due to physicochemical adsorption (chemisorption) to the hydroxyapatite structure of bone tissue (*19*). Using autoradiography, the deposition of ^{99m}Tc-diphosphonates was found to occur at the mineralization front of bone (osteoid) and at the osteocytic lacunae, but not near osteoclasts (*20*). In the growing skeleton, mineral deposition is predominantly seen at epiphyseal growth plates and osteochondral junctions (*21*).

In contrast to ^{99m}Tc-diphosphonates, a certain fraction of extravascular fluoride is directly incorporated into the

bone matrix, because fluoride ions exchange with hydroxyl groups in the hydroxyapatite crystal of bone to form fluoroapatite (*22*). One would therefore expect the net transport of fluoride into bone to be closely related to bone metabolism. In fact, dynamic ^{18}F-NaF provides quantitative estimates of bone metabolism (via net transport constant) that correlate well with the mineral apposition rate obtained from bone histomorphometry (*18,23*), the most accurate method for the investigation of bone formation. Bone histomorphometry provides several static parameters that are important in assessing the microarchitecture of bone. The dynamic parameter that quantitatively reflects bone formation, the mineral apposition rate, requires double-tetracycline labeling of bone biopsy samples. In addition, bone histomorphometry is an invasive procedure requiring sedation and can sample only a single site of bone, usually the iliac crest. In clinical practice, bone histomorphometry is substituted with biochemical serum markers of bone metabolism, including alkaline phosphatase, and urinary N-telopeptide and C-telopeptide of collagen cross-links (*3*). Although such markers display relatively rapid treatment-induced changes, they are significantly limited by large day-to-day variations and insensitivity to regional changes because they reflect bone metabolism of the entire skeleton (*24*). Therefore, quantitative imaging of bone metabolism is of considerable interest for specialized clinical indications. The above data indicate that noninvasive dynamic ^{18}F-NaF PET with determination of the net transport constant of ^{18}F-NaF to bone is indeed a suitable surrogate marker of the mineral apposition rate.

Renal Excretion

^{99m}Tc-diphosphonate compounds belong to the class of bisphosphonates, which are not significantly metabolized in vivo (*25*). Thus, renal excretion is the primary route for their elimination. Hyldstrup et al. showed that the renal filtration fraction of free (non–protein-bound) ^{99m}Tc-MDP is the same as that for ^{51}Cr-ethylenediamine tetraacetic acid, itself a measure of the glomerular filtration rate (*26*); thus, the renal elimination rate of ^{99m}Tc-diphosphonates depends mainly on glomerular function. Since the plasma binding of ^{18}F-NaF is small, fluoride ions are freely filtered in the glomeruli. Fluoride, however, also undergoes tubular reabsorption. As a result, renal clearance of ^{18}F-NaF is dependent on overall urinary flow, because tubular reabsorption of fluoride increases with decreasing glomerular filtration rate (*3*). Therefore, it is recommended that patients undergoing ^{18}F-NaF PET be well hydrated to reduce radiation exposure.

Environmental Factors

Other environmental factors may influence the accumulation of ^{99m}Tc-MDP and ^{18}F-NaF as well. Although renal clearance of ^{18}F-NaF is modulated by urinary pH and diet, renal clearance of ^{99m}Tc-MDP is affected by phosphate concentration and pH (*27*). Also, the adsorption of ^{99m}Tc-MDP to hydroxyapatite appears to increase at low pH (*28*).

Quantification Methods

Short-lived radiotracers such as ^{99m}Tc-labeled diphosphonates and ^{18}F-NaF allow for kinetic modeling, which provides simplified mathematic models to quantitatively describe aspects of bone perfusion and metabolism. Quantitative analysis of bone turnover is of interest for evaluation of conditions with diffuse alteration to bone remodeling (such as primary hyperparathyroidism, renal osteodystrophy, and osteoporosis), and for assessment of bone perfusion, to assess bone (graft) vitality and osteonecrosis.

Quantitative bone scintigraphy was developed with ^{99m}Tc-MDP to study metabolic bone disorders with global effects on the skeleton. A simple parameter is 24-h whole-body bone retention, $K_{bone}/(K_{bone} + K_{renal})$ (*8*), where K_{bone} and K_{renal} denote the respective clearance of radioactivity from bone and renal plasma. These parameters can be measured by either a γ-camera or 24-h urine collection.

Although regional uptake measures are possible when combined with γ-camera imaging, whole-body bone retention represents an estimate for the entire skeleton. The whole-body bone retention method has several limitations. It assumes that radioactivity bound to bone will not dissociate from bone and that radioactivity in soft tissues is negligible at 24 h; these assumptions may not hold true. Nevertheless, in metabolic bone diseases, whole-body bone retention varies from normal values—decreasing in osteoporosis and increasing in renal osteodystrophy, Paget disease, osteomalacia, and primary hyperparathyroidism (*3*). When serial γ-camera imaging is combined with blood sampling, it is possible to measure ^{99m}Tc-MDP plasma clearance for the whole skeleton and for selected regions of interest (*29*). However, because of the variable degree of protein binding of ^{99m}Tc-MDP, ultrafiltration of plasma samples is necessary for accurate quantification. Despite general availability and relative model simplicity, quantitative bone scintigraphy has not gained widespread acceptance for clinical use, probably because of the availability of serum markers providing similar clinical information.

PET imaging with ^{18}F-NaF has several advantages over quantitative methods using ^{99m}Tc-MDP bone scanning. In contrast to γ-camera imaging, including SPECT, PET allows for absolute quantification of radioactivity per measured volume. Quantitative analysis of ^{18}F-NaF PET requires dynamic imaging and serial measurements of radioactivity in blood to obtain an input function, ideally from arterial blood. Hawkins et al. developed a 2-tissue, 3-compartment model (*30*), which in addition to a vascular compartment consists of bound and unbound bone compartments. The negatively charged fluoride anion, F^-, diffuses into the extravascular (unbound bone) space. A certain fraction will then be further bound to the bone matrix and incorporated as fluoroapatite (F-apatite). The model has 5 variable parameters: 4 rate constants and 1 constant for the vascular compartment. The rate constants describing these processes are as follows: K_1 and k_2 for the forward and reverse capillary transport, k_3 for the binding

to the bone matrix, and k_4 for the release reaction (Fig. 2). The magnitude of k_4 is typically small in comparison to k_2 and k_3, indicating little dissociation of fluoride from the bone matrix. Within this model, the net transport of ^{18}F-NaF into bone (commonly called K_i) is proportional to the term $K_1 \cdot k_3/(k_2 + k_3)$, which can be obtained graphically (known as the Patlak plot). Accordingly, the fraction of tracer in the extravascular space that undergoes binding to bone mineral can be described by the term $k_3/(k_2 + k_3)$ (*31*).

An important advantage of compartmental modeling is that all individual rate constants (microparameters) and the net transport of ^{18}F-NaF into bone (macroparameter) can be estimated; thus, bone blood flow, fluoride binding to bone mineral, and overall bone metabolism can be assessed at the same time. However, compartmental modeling approaches have demanding requirements. Dynamic PET requires a relatively long acquisition time of typically 60 min. Accordingly, the available field of view will be rather limited. Furthermore, arterial blood sampling and challenging data quality control are required to obtain precise estimates of microparameters. These issues have clearly limited clinical applications.

The computationally less demanding graphical method (Patlak plot) assumes that the release of radioactivity from the bone compartment is negligible. In many physiologic situations and low-turnover bone diseases, this assumption is valid. Since measurement errors are often lower with the graphical method than with compartment modeling, fewer subjects may be required to determine a statistically significant change (*32*). However, the Patlak plot provides only measurements for K_i and still requires a measured blood input function.

Various simplifications to this kinetic modeling approach have been proposed and tested. Arterial blood sampling can be avoided by substituting the arterial measurements with either population-derived input functions (*33*) or semi–population-derived input functions (*34*) requiring only a small number of additional venous blood samples. Image-derived input functions are an attractive alternative but are limited by the available field of view. Puri et al. examined various methods for quantification of K_i at the hip and lumbar spine, including 2-tissue-compartment 4-parameter, 2-tissue-compartment 3-parameter, and Patlak plots, and compared these with standardized uptake value (SUV) measurements (*32*). The measurement of SUV is comparatively simple as it can be obtained from static images without any blood sampling; however, it does not account for variable radiotracer clearance from the vascular space. Although statistically significant correlations between all quantification methods were reported, the data should be interpreted with caution as they were obtained only in healthy volunteers. Brenner et al. investigated compartmental modeling, Patlak plots, and SUV in a wide range of normal and pathologic bone conditions and confirmed strong correlations among methods (*35*). However, high variability was found for SUV measurements, indicating limited accuracy in cases of low metabolic bone turnover.

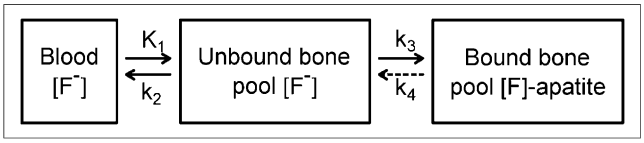

FIGURE 2. An ^{18}F-NaF 2-tissue-compartment model (3 compartments and 4 parameters).

Dosimetry of ^{99m}Tc-MDP and ^{18}F-NaF

In adults, the whole-body exposure from ^{18}F-NaF administration is 0.024 mSv/MBq. Therefore, for a standard 370-MBq (10-mCi) ^{18}F-NaF PET scan, the effective dose is 8.9 mSv. This compares with an adult ^{99m}Tc-MDP whole-body exposure of 0.0057 mSv/MBq, resulting in an effective dose of 5.3 mSv for a 925-MBq (25-mCi) administration (*6*). For ^{18}F-NaF, the organ receiving the highest radiation dose is the bladder, whereas ^{99m}Tc-MDP has higher exposure to bone surfaces.

CLINICAL APPLICATIONS

Dynamic (3-phase) bone scanning involves an angiographic flow phase (typically using 1- to 3-s frames for 60 s after radiotracer injection), a soft-tissue phase (at 5–15 min), and a delayed phase (usually performed at 3–4 h) to allow for sufficient radiotracer clearance from soft tissues and radiotracer binding to bone (*36*). The second phase, often inaccurately described as the blood-pool phase, is obtained during a major shift of radiotracer from the blood to the extracellular space and then to target and nontarget tissues. Therefore, depending on the particular timing of this acquisition, commonly a significant amount of the radiotracer has already cleared from the blood, and the phase is therefore better referred to as the soft-tissue phase. Second- and third (delayed)-phase imaging can be performed using a whole-body technique to obtain whole-body soft-tissue and delayed bone-uptake images. Improvements to the technique have been made with SPECT imaging and the more recent combination of functional and anatomic imaging with SPECT/CT (*37*).

Typical quantitative dynamic PET imaging requires imaging of the same bed position for at least 60 min. For routine clinical applications, ^{18}F-NaF PET (or PET/CT) could, however, be performed similarly to a 3-phase bone scan by obtaining a short (0–10 min) dynamic acquisition of an area of interest, which would represent both the angiographic flow and the soft-tissue phases of the 3-phase bone scan. Because ^{18}F-NaF displays more rapid kinetics than does ^{99m}Tc-MDP, this dynamic scan can be relatively short. At around 60 min after injection, a whole-body acquisition representing the late-phase scan would follow. Although the utility of such an approach has not been tested and would depend on the particular technical characteristics of the PET scanner used, the approach would be expected to provide meaningful semiquantitative data that could replace a 3-phase bone scan at a fraction of time.

Bone Viability

Three-phase bone scanning is a suitable method to evaluate bone viability, an important factor for uncomplicated healing of vascularized bone grafts (*38–40*). Bone scintigraphy performed early (days 2–11) after surgery allows assessment of graft microperfusion, with graft survival reliant on intact blood flow during this critical period (*38*). Early bone scanning avoids false-positive results due to periosteal uptake along the graft surface and rare cases of late osteonecrosis presenting with uptake. Increased uptake in the graft predicts an uncomplicated healing course. Conversely, photopenia indicates vascular occlusion, which is followed by necrosis and graft failure (*39*). In a study investigating vascularized fibula grafts for repair of mandibular defects, uptake was present in 12 of 13 grafts with uncomplicated healing, whereas 3 failed grafts had decreased uptake (*38*). The technique can be improved with SPECT/CT imaging (Fig. 3) and semiquantitative analysis such as the measurement of transplant-to-cranium ratios, with values greater than 1.0 reported to have a high predictive value for successful healing (*41*). Three-phase bone scans were used to assess the vitality of vascularized femur allografts, with hyperemia indicating excellent perfusion and patency of transplanted vessels, and suitable uptake at 12 mo predicting a healthy graft (*40*). ^{99m}Tc-MDP bone scans have also been used to monitor new bone formation of the mandible during distraction osteogenesis for the treatment of hemimandibular abnormalities (*42*). A low level of bone uptake was suggestive of impending nonunion, requiring a decrease in the rate of distraction to allow healing.

In contrast to 3-phase bone scans, ^{18}F-NaF PET allows quantitative measurements of bone blood flow and metabolism (*43*). Figure 4 demonstrates a case of a vascularized fibula graft after resection of a primary osteosarcoma of the femur shaft. Dynamic ^{18}F-NaF PET of the transplant with proximal hypertrophic nonunion reveals significant differences in estimates for K_1 and K_i, indicating impaired perfusion and metabolic function of the fibula transplant. Schliephake et al. used ^{18}F-NaF PET to assess the viability of vascularized fibula grafts for mandibular reconstructions and reported that increased uptake (average of 19 d after surgery) within the graft and union sites, as compared with a cervical bone reference, indicted successful healing (*44*). In another study, graft failures were associated with near-zero fluoride influx into the fibula graft on ^{18}F-NaF PET (*45*).

Incorporation of cryopreserved allogenic bone graft material is uncertain as it has been shown to suffer from ineffective osteoinduction and osteoconduction (*46*). Previously, we used dynamic ^{18}F-NaF PET to evaluate the biologic fate of allogenic bone grafts used to augment hip revision arthroplasties (*47*). That study revealed the presence of host bone formation in allogenic bone grafts early after surgery. Temmerman et al., using both ^{15}O-H_2O PET and ^{18}F-NaF PET, investigated bone blood flow and metabolism in patients undergoing total hip revision arthroplasty using allogenic bone grafts (*48*). This pilot study revealed

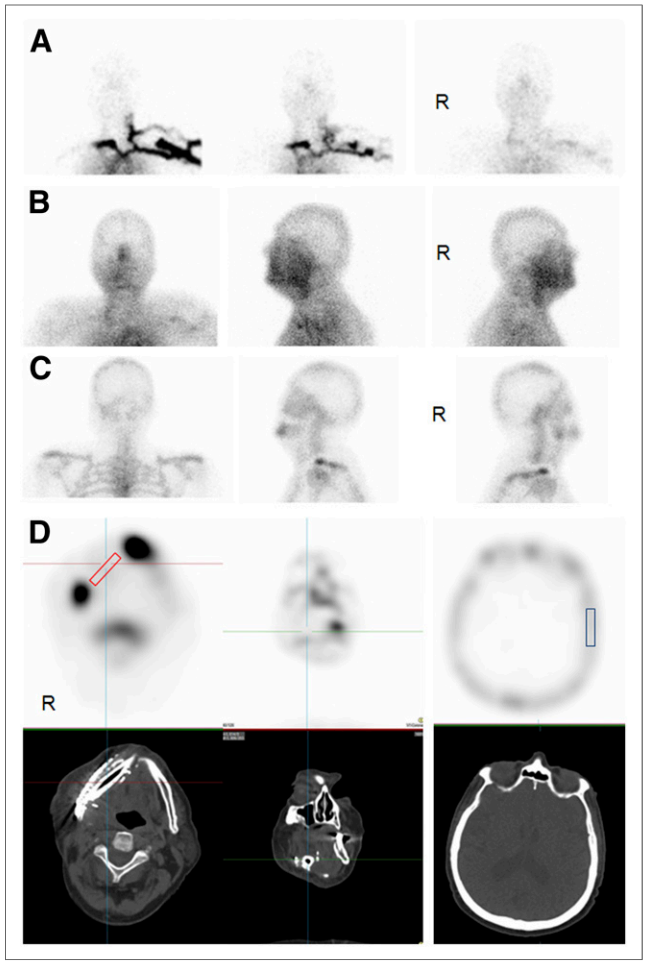

FIGURE 3. ^{99m}Tc-MDP bone scan for viability assessment of vascularized fibula graft in patient with osteonecrosis of jaw. On anterior, left, and right planar projections, angiographic (A) and soft-tissue (B) phases show nonspecific diffuse hyperemia overlying mandible due to surgical trauma. Delayed planar images (C) display focal increased uptake at genuine mandible near union sites of fibula graft. Transaxial and coronal SPECT/CT reveals photopenia in graft region (D). Regions of interest are defined in fibula graft (red) and calvarium (blue) on 3 consecutive slices to calculate graft-to-calvarium uptake ratio (41). Visual inspection and ratio result (0.72) are suggestive of nonviable graft.

that areas of allogenic bone grafts displayed increased blood flow and metabolism as early as 2 wk after surgery that stabilized 3 mo after treatment, indicating new bone formation. Their observation of continued coupling of bone blood flow and metabolism was similar to our findings in allogenic bone grafts (*47*) and high-turnover bone disease (*18*). In an elegant PET study, Sörensen et al. evaluated bone blood flow (with ^{15}O-H_2O), bone blood volume (with ^{15}O-carbon monoxide), and bone metabolism using ^{18}F-NaF serially—8 d and 12 mo after surgery—to investigate incorporation of cryopreserved morselized allografts in total-hip arthroplasties (*49*). Their results indicated that blood flow and bone metabolism in allografts showed early increases that normalized 12 mo after surgery in patients

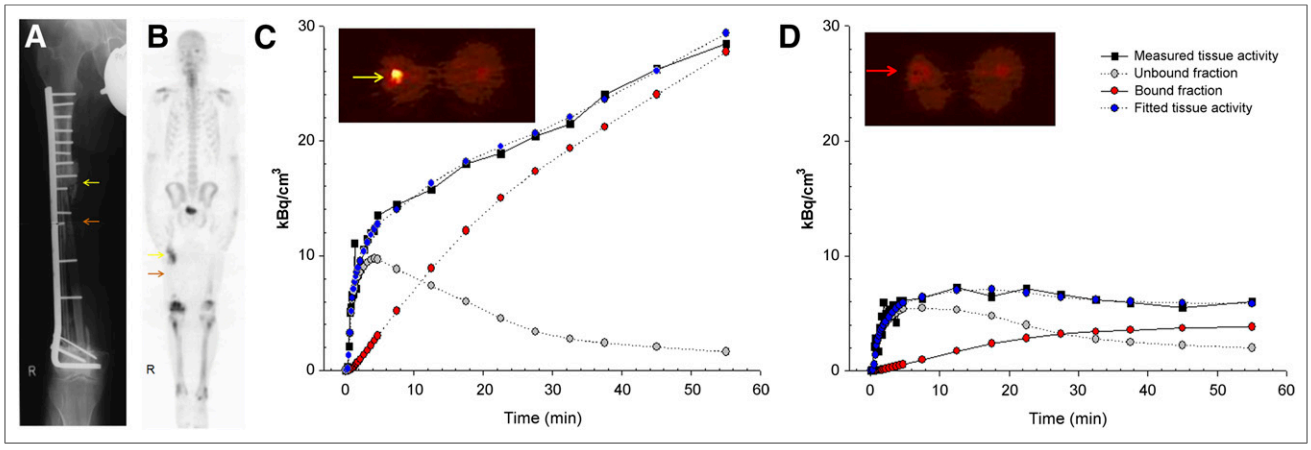

FIGURE 4. Plate fixation of vascularized fibula transplant (red arrow) after resection of osteosarcoma of right femur (A). Revision plate fixation was performed after fracture due to nonunion (yellow arrow). After injection of 370 MBq of ^{18}F-NaF, dynamic PET study of mid thigh was performed for 60 min, followed by non–attenuation-corrected whole-body scan (B). Attenuation-corrected and axial slices (50–60 min) of hypertrophic nonunion (C) and fibular graft (D) areas show markedly increased uptake at nonunion and decreased uptake at level of fibula graft. Tissue time–activity curves (black squares) demonstrate rapid and sustained net-accumulation of radiotracer in nonunion but poor accumulation in fibula graft. Compartmental modeling was performed, providing estimates for total tissue activity (blue dots) and fraction of bound (red dots) and unbound (gray dots) radiotracer in tissue. At later time points, relationship of bound to unbound radiotracer is much higher in hypertrophic nonunion (C) than in failing graft (D).

with a successful clinical outcome. Although ^{18}F-NaF PET is highly predictive of bone viability and surgical outcome, it remains uncertain whether observed increases in bone blood flow and metabolism can be attributed entirely to new bone formation and whether this bone formation is related to the host's own osteoblasts or to osteoblasts originating from grafted tissues (*50*).

Osteonecrosis and Avascular Necrosis

Numerous studies have documented the usefulness of 3-phase bone scans for evaluation of avascular necrosis of the femoral head due to trauma, a slipped capital femoral epiphysis, steroid use, radiation effects, sickle cell disease, or Perthes disease, with accuracies exceeding 95% (Fig. 5) (*9,36*). Initial photopenia of the femoral head indicating interruption of blood flow is followed either by necrosis or subsequent reossification and healing response if revascularization occurs. Dasa et al. investigated 11 patients with nontraumatic osteonecrosis of the femoral head (*51*). Nine of 17 hips had increased acetabular ^{18}F-NaF uptake not identified with bone scans, including SPECT, or with MR imaging, indicating that ^{18}F-NaF may reveal changes earlier than traditional imaging. In a pilot study, Schiepers et al. used ^{18}F-NaF PET/CT to predict healing of femoral head osteonecrosis by conservative measures based on blood flow estimates derived from ^{18}F-NaF (*52*). A study performing ^{18}F-NaF PET/CT after resurfacing arthoplasty found that lack of uptake in the femoral head was indicative of poor vascularity and subsequent osteonecrosis (*53*).

Serial Bone Imaging at Multiple Time Points

Pathophysiology of Bone Metastases. Disseminated tumor cells that successfully invade bone depend on adhesion mechanisms, interacting with the extracellular matrix, stromal cells, osteoblasts, osteoclasts, and endothelial cells to promote tumor cell survival (*54*). To form clinically overt metastases, tumor cells must be able to either stimulate cellular proliferation or attenuate micrometastatic mass dormancy programs. Phenotypically, bone metastases present as osteolytic (bone resorbing), osteoblastic (bone forming), or a mixture of both. As recently reviewed (*55*), these phenotypes are determined via a complex web of interactions among cancer cells, bone, and T-cells, a process that is mediated by many soluble factors and transcriptional activities that ultimately regulate osteolysis and osteoblastogenesis.

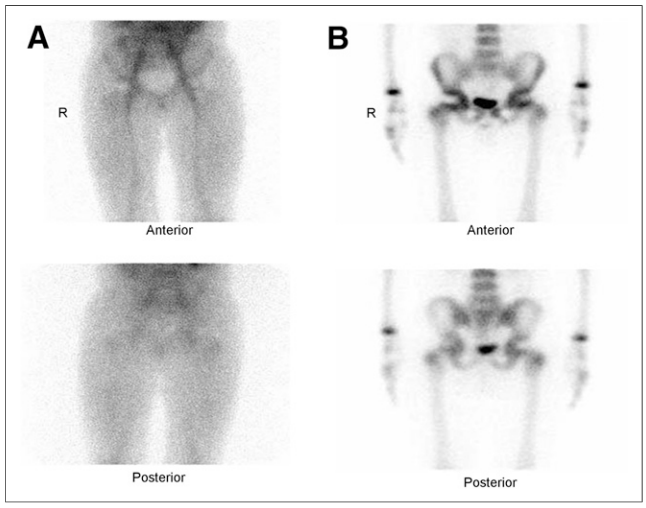

FIGURE 5. An 8-y-old boy with right hip pain and avascular necrosis of right femur head (Legg-Calve-Perthes disease). Anterior and posterior projection soft-tissue (A) and delayed-phase images (B) show focally decreased ^{99m}Tc-MDP uptake in right femoral head.

Staging of Bone Metastases. Bone scans are sensitive, cost-effective, whole-body imaging modalities for staging cancers that have a predilection for bone metastases (*9*), with overall sensitivity between 62% and 100% and specificity of 78%–100% (*56*). However, false-negative studies are commonly seen with osteolytic lesions, resulting in poor sensitivity (as low as 50% for myeloma). Use of SPECT/CT has been shown to improve specificity, with a reduced number of indeterminate bone lesions (compared with planar imaging) for staging of lung cancer bone metastases (*37*).

^{18}F-FDG PET/CT for oncologic staging is highly sensitive for detection of bone metastases. For staging of lung cancer skeletal metastases, a metaanalysis that included 7 studies (1,794 patients) reported ^{18}F-FDG PET sensitivity of 98% and specificity of 95%—superior to the conventional bone scan sensitivity of 87% and specificity of 82% (*56*). On imaging, osteoblastic, osteoclastic, or mixed phenotypes lead to mainly sclerotic, lytic, or mixed lesions, respectively. The predominant phenotype affects the detection potential of radiotracers. Thus, ^{18}F-FDG PET has higher sensitivity for early marrow metastases and lytic lesions than do bone-seeking tracers.

^{18}F-NaF PET is a highly sensitive method for detection of primary bone tumors (*5*) and osseous metastatic disease from a range of primary tumors, including lung, breast, prostate, thyroid, and squamous cell cancers of the head and neck (*3,5,6*). Generally, increased ^{18}F-NaF uptake is found in sclerotic and mixed lesions and at cortical locations (*57*). ^{18}F-NaF PET has superior sensitivity to ^{99m}Tc-labeled diphosphonate bone scanning using planar and SPECT protocols (*5*). When combined with hybrid PET/CT imaging, ^{18}F-NaF was able to clarify many findings otherwise equivocal on conventional bone scanning (*58*). Krüger et al. compared ^{18}F-NaF PET with ^{18}F-FDG PET and ^{99m}Tc-MDP bone scanning in 126 patients with non–small cell lung cancer. ^{18}F-NaF PET was superior in sensitivity to ^{99m}Tc-MDP and comparable to ^{18}F-FDG PET (*59*). For biochemical relapse of prostate cancer, ^{18}F-NaF appears to have greater diagnostic yield than ^{18}F-FDG (*60*). In a comparative study between ^{18}F-NaF PET and ^{18}F-choline PET, ^{18}F-NaF resulted in higher numbers of detected bone metastases, although detection of additional sites of disease did not alter management (*61*). ^{18}F-NaF uptake may display a posttreatment flare phenomenon, similar to that reported in ^{99m}Tc-MDP bone scans (*5*).

Therapeutic Response Evaluation. In recent years, several promising systemic treatments for castration-resistant prostate cancer have been developed (*62*). In particular for progression after docetaxel chemotherapy, various mechanisms have been exploited, including cabazitaxel (second-generation taxane), abiraterone (targeting androgen-receptor signaling), ^{223}Ra-chloride (α-particle emitter with calcium-mimetic high bone affinity), cabozantinib (tyrosine kinase inhibitor with activity against Met and vascular endothelial growth factor receptor 2), sipuleucel-T (immunotherapy and autologous dendritic cell therapy), and enzalutamide, many of which have shown survival benefits in clinical trials (*62*). Because development of these agents is expensive, objective proof of efficacy will be necessary using both biochemical and imaging biomarkers.

Conventional bone scans have several limitations for therapy response assessment. Unlike ^{18}F-FDG, which targets the glucose consumption within tumors, bone-seeking radiotracers reflect the metabolic response of bone tissue to the presence of metastases. Thus, at best they represent an indirect measurement of tumor response. Consequently, even after successful systemic treatment of bone metastases, bone scans are known to improve very slowly, if at all (*63*). Other notable problems are false-negative results, a flare response leading to worsening of the scan appearance despite a clinical response to therapy, poor interobserver agreement, subjective interpretation, and inability to grade changes in intensity and extent (*63,64*). Also, certain chemotherapeutic approaches may directly interfere with bone remodeling. For example, the anti-RANKL (receptor activator of nuclear factor κB ligand) monoclonal antibody denosumab inhibits osteoclast function (*65*), which interferes with the ability to assess response on bone scans. Figure 6 illustrates that after denosumab treatment there is near-complete normalization of bone scan findings, although this may simply reflect inhibition of osteoclast function rather than an objective clinical response.

A ^{99m}Tc-MDP bone scan index has been proposed as an imaging biomarker to improve the reproducibility of treatment response assessment. This index aims to quantify tumor burden as a percentage of the total skeletal mass of a reference man (*63*). Bone scan index and bone scan index doubling time measurements have been shown to correlate with outcome in clinical trials for castration-resistant prostate cancer (*63,64*). Computer-aided quantitative intensity normalization and segmentation of bone uptake compared with healthy controls has also been proposed to assess therapy response after cabozantinib treatment (measuring lesion area and numbers as well as radiotracer uptake per lesion) (*64*).

Although the ability to perform quantitative analysis in response evaluations is a key advantage of ^{18}F-NaF PET over conventional bone scanning, it has rarely been applied in clinical trials. Dynamic ^{18}F-NaF PET and kinetic modeling was used in breast cancer bone metastases to measure K_1 and K_i, a potential technique for assessment of treatment response (*66*). Clearly, the requirement for a limited field of view for dynamic ^{18}F-NaF PET is undesirable. Therefore, semiquantitative analyses of SUVs obtained from static whole-body ^{18}F-NaF PET acquisitions were used to assess response to ^{223}Ra-dichloride treatment. In a small pilot study, ^{18}F-NaF SUV appeared to have predictive value for evaluating the response of prostate cancer bone metastases, whereas qualitative (visual) interpretation tended to be less valuable (*67*). These initial results demonstrate the potential for quantitative approaches to monitor treatment response using ^{18}F-NaF PET.

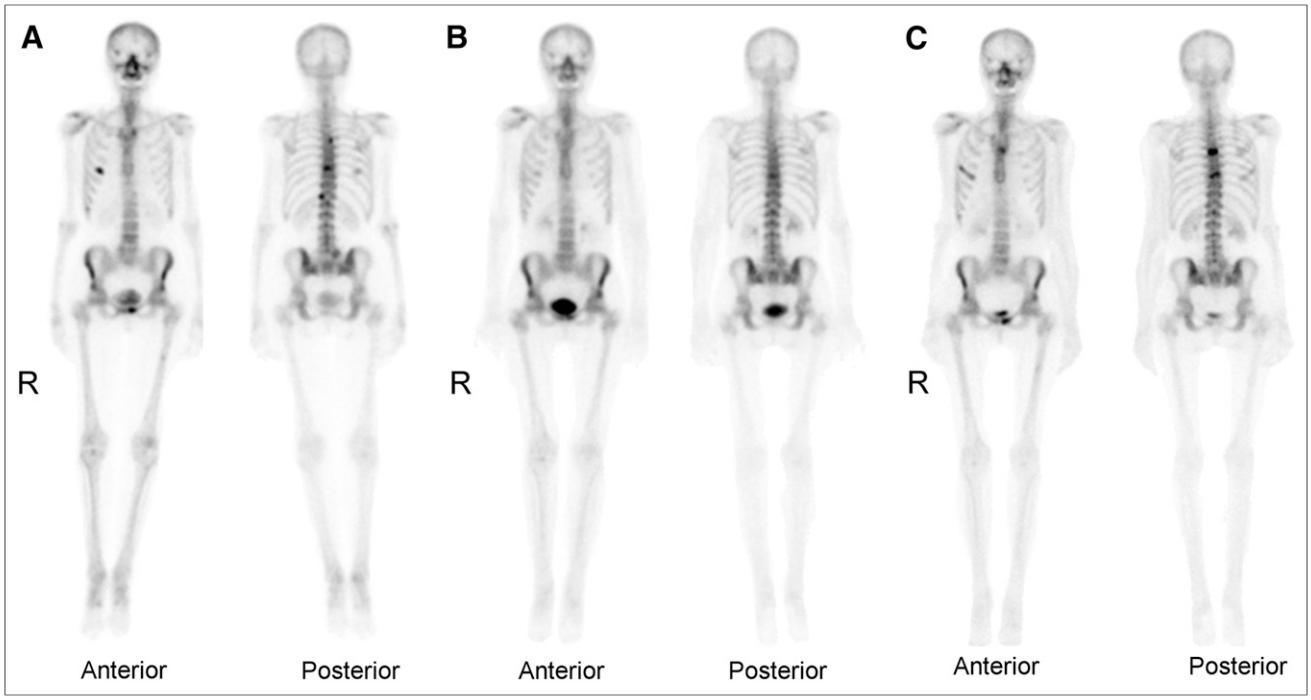

FIGURE 6. Breast cancer bone metastases identified on anterior and posterior projection whole-body bone scan in ribs, spine, pelvis, and left femur shaft (A). Treatment with denosumab results in near-normalization of scan findings (B), although with continued rise of tumor marker CA15-3. Three months after treatment, bone scan again identifies apparent disease progression (C).

Benign Metabolic Bone Disorders

Paget disease is an idiopathic disorder characterized by accelerated bone turnover with abnormally increased osseous formation and resorption. Quantitative methods on bone scintigraphy provide noninvasive measurements of bone turnover that have been shown to correspond to serum and urinary markers of bone turnover (*68,69*). Polyostotic Paget disease is characterized by increased global skeletal uptake, compared with healthy controls (*69*). The whole-body bone index is a parameter developed for objective characterization of the extent of polyostotic Paget disease to allow comparison on serial studies to assess treatment response (*68*). In metabolic bone disorders such as primary hyperparathyroidism, bone scans typically show diffuse increased uptake throughout the skeleton and may result in a "superscan" appearance (*9*). Also, quantitative bone scintigraphy demonstrated increased bone turnover in 51% of patients with primary hyperparathyroidism and in 78% of patients with thyrotoxicosis, compared with healthy controls (*70*).

Paget disease has been studied with dynamic ^{18}F-NaF PET/CT using compartmental modeling, which confirmed increased net fluoride influx to pagetic bone; involved vertebral bodies displayed increased K_1 and K_i values compared with normal vertebrae (*71*). In hereditary hyperostosis cranialis interna, ^{18}F-NaF PET/CT was used to quantify bone metabolism in the skull base of affected patients and provided information about disease severity and pattern of involvement (*72*). Dynamic ^{18}F-NaF PET has also been used to study metabolic bone diseases. In renal osteodystrophy, a common cause for secondary hyperparathyroidism, there was increased bone metabolism (increased K_i) in affected patients compared with healthy subjects (*23*). After parathyroidectomy and medical management, bone metabolism (K_i) decreased between 30% and 40%, demonstrating the ability to monitor treatment response. In an experimental porcine model of parathyroid hormone–related high-turnover bone disease, dynamic ^{18}F-NaF PET allowed the detection of high-turnover osteopenia after gastrectomy in mini pigs (*73,74*). Furthermore, the combination with quantitative CT bone densitometry allowed normalization of metabolic changes by the specific bone mass, thus increasing the discriminatory power in metabolic bone diseases (*74*).

Quantitative dynamic ^{18}F-NaF PET/CT has also been performed for the investigation of low-turnover bone diseases, including osteoporosis (*75*), and to assess age-related changes in pre- and postmenopausal women (*76*). In a large study performed by Frost et al., dynamic ^{18}F-NaF PET and bone mineral densitometry were performed on 72 postmenopausal women classified as having normal, osteopenic, or osteoporotic bones (*31*). Bone metabolism (K_i) and fluoride binding to bone mineral [$k_3/(k_2 + k_3)$] were significantly reduced in osteoporosis, whereas at the same time biochemical markers of bone turnover (bone-specific alkaline phosphatase) were increased. This somewhat surprising result highlights the importance of regional measurements of bone turnover (from imaging) to improve the understanding of metabolic bone diseases.

Bisphosphonate Treatment-Response Evaluation

The availability of effective treatments for Paget disease, osteoporosis, and bone metastases has led to renewed interest in quantitative imaging of bone metabolism to assess response. Bisphosphonates are biologically stable analogs of pyrophosphates that have a high affinity for hydroxyapatite and induce apoptosis of osteoclasts, thereby inhibiting bone resorption (*77*). In monoostotic Paget disease, serum biomarkers are often within the reference range. Accordingly, regional bone scanning has been used to assess response to bisphosphonate treatments, including comparative analysis of bisphosphonate (risedronate and tiludronate) treatments (*78*).

^{18}F-NaF PET offers the ability to monitor the response to bisphosphonate treatment quantitatively. In 14 patients with Paget disease, bone metabolism as measured by K_i (obtained from nonlinear regression and Patlak analysis) and by SUV obtained from static ^{18}F-NaF PET significantly decreased after bisphosphonate treatment (*79*). This study indicated that simple SUV measurements may be sufficient for monitoring disease response in metabolic bone diseases. After alendronate treatment of osteoporosis, decreases in serum alkaline phosphatase were seen, along with decreasing ^{18}F-NaF SUV measurements in lumbar spine and femoral sites, associated with increases in bone mineral density on dual-energy x-ray absorptiometry (*80*). Therefore, simplified measurement of SUV on static ^{18}F-NaF PET/CT promises to improve clinical application.

CONCLUSION

Because of similarities between the uptake mechanisms of ^{99m}Tc-labeled diphosphonates and ^{18}F-NaF, routine clinical use of whole-body ^{18}F-NaF PET can be quickly implemented. Quantitative measurements of bone blood flow and metabolism with ^{18}F-NaF PET have been instrumental to our understanding of metabolic bone diseases and bone regeneration after surgical interventions. Treatment-induced changes to bone metabolism provide an impetus for using ^{18}F-NaF PET to assess response to antiresorptive bisphosphonate treatments and novel therapies of bone metastases. Clearly, the necessity for dynamic image acquisition has limited clinical applications of quantitative ^{18}F-NaF PET, an otherwise highly sensitive and accurate imaging approach. Initial reports indicating that simplified ^{18}F-NaF SUV uptake measurements may be suitable substitutes for more complex kinetic modeling are therefore encouraging.

REFERENCES

1. Blau M, Nagler W, Bender MA. Fluorine-18: a new isotope for bone scanning. *J Nucl Med.* 1962;3:332–334.
2. Hoh CK, Hawkins RA, Dahlbom M, et al. Whole body skeletal imaging with [^{18}F]fluoride ion and PET. *J Comput Assist Tomogr.* 1993;17:34–41.
3. Blake GM, Park-Holohan SJ, Cook GJ, Fogelman I. Quantitative studies of bone with the use of ^{18}F-fluoride and ^{99m}Tc-methylene diphosphonate. *Semin Nucl Med.* 2001;31:28–49.
4. Czernin J, Satyamurthy N, Schiepers C. Molecular mechanisms of bone ^{18}F-NaF deposition. *J Nucl Med.* 2010;51:1826–1829.
5. Grant FD, Fahey FH, Packard AB, Davis RT, Alavi A, Treves ST. Skeletal PET with ^{18}F-fluoride: applying new technology to an old tracer. *J Nucl Med.* 2008; 49:68–78.
6. Segall G, Delbeke D, Stabin MG, et al. SNM practice guideline for sodium ^{18}F-fluoride PET/CT bone scans 1.0. *J Nucl Med.* 2010;51:1813–1820.
7. Turner CH. Bone strength: current concepts. *Ann N Y Acad Sci.* 2006;1068:429–446.
8. Einhorn TA. The bone organ system: form and function. In: Marcus R, Feldman D, Kelsey J, eds. *Osteoporosis*. San Diego, California: Academic Press; 1996:3–22.
9. Brenner AI, Koshy J, Morey J, Lin C, DiPoce J. The bone scan. *Semin Nucl Med.* 2012;42:11–26.
10. Blake GM, Moore AE, Fogelman I. Quantitative studies of bone using ^{99m}Tc-methylene diphosphonate skeletal plasma clearance. *Semin Nucl Med.* 2009; 39:369–379.
11. Piert M, Zittel TT, Machulla HJ, et al. Blood flow measurements with [^{15}O]H_2O and [^{18}F]fluoride ion PET in porcine vertebrae. *J Bone Miner Res.* 1998; 13:1328–1336.
12. Renkin EM. Transport of potassium-42 from blood to tissue in isolated mammalian skeletal muscles. *Am J Physiol.* 1959;197:1205–1210.
13. Hughes SP, Davies DR, Bassingthwaighte JB, Knox FG, Kelly PJ. Bone extraction and blood clearance of diphosphonate in the dog. *Am J Physiol.* 1977;232: H341–H347.
14. Fogelman I. Skeletal uptake of diphosphonate: a review. *Eur J Nucl Med.* 1980;5:473–476.
15. McCarthy ID, Hughes SP. The role of skeletal blood flow in determining the uptake of ^{99m}Tc-methylene diphosphonate. *Calcif Tissue Int.* 1983;35:508–511.
16. Heinonen I, Kemppainen J, Kaskinoro K, et al. Bone blood flow and metabolism in humans: effect of muscular exercise and other physiological perturbations. *J Bone Miner Res.* December 21, 2012 [Epub ahead of print].
17. Herscovitch P, Raichle ME, Kilbourn MR, Welch MJ. Positron emission tomographic measurement of cerebral blood flow and permeability-surface area product of water using [^{15}O]water and [^{11}C]butanol. *J Cereb Blood Flow Metab.* 1987;7:527–542.
18. Piert M, Zittel TT, Becker GA, et al. Assessment of porcine bone metabolism by dynamic [^{18}F]fluoride ion PET: correlation with bone histomorphometry. *J Nucl Med.* 2001;42:1091–1100.
19. Francis MD, Ferguson DL, Tofe AJ, Bevan JA, Michaels SE. Comparative evaluation of three diphosphonates: in vitro adsorption (C-14 labeled) and in vivo osteogenic uptake (Tc-99m complexed). *J Nucl Med.* 1980;21:1185–1189.
20. Einhorn TA, Vigorita VJ, Aaron A. Localization of technetium-99m methylene diphosphonate in bone using microautoradiography. *J Orthop Res.* 1986;4:180–187.
21. Christensen SB, Krogsgaard OW. Localization of Tc-99m MDP in epiphyseal growth plates of rats. *J Nucl Med.* 1981;22:237–245.
22. Grynpas MD. Fluoride effects on bone crystals. *J Bone Miner Res.* 1990;5(suppl 1):S169–S175.
23. Messa C, Goodman WG, Hoh CK, et al. Bone metabolic activity measured with positron emission tomography and [^{18}F]fluoride ion in renal osteodystrophy: correlation with bone histomorphometry. *J Clin Endocrinol Metab.* 1993;77: 949–955.
24. Blake GM, Frost ML, Fogelman I. Quantitative radionuclide studies of bone. *J Nucl Med.* 2009;50:1747–1750.
25. Lin JH. Bisphosphonates: a review of their pharmacokinetic properties. *Bone.* 1996;18:75–85.
26. Hyldstrup L, McNair P, Ring P, Henriksen O. Studies on diphosphonate kinetics. Part I: evaluation of plasma elimination curves during 24 h. *Eur J Nucl Med.* 1987;12:581–584.
27. Okamoto YM. Mechanism of accumulation of ^{99m}Tc-MDP to bone: correlation of in vivo data with in vitro data. *Radiat Med.* 1997;15:209–215.
28. Okamoto Y. Accumulation of technetium-99m methylene diphosphonate: conditions affecting adsorption to hydroxyapatite. *Oral Surg Oral Med Oral Pathol Oral Radiol Endod.* 1995;80:115–119.
29. Moore AE, Blake GM, Fogelman I. Validation of a blood-sampling method for the measurement of ^{99m}Tc-methylene diphosphonate skeletal plasma clearance. *J Nucl Med.* 2006;47:581–586.
30. Hawkins RA, Choi Y, Huang SC, et al. Evaluation of the skeletal kinetics of fluorine-18-fluoride ion with PET. *J Nucl Med.* 1992;33:633–642.
31. Frost ML, Fogelman I, Blake GM, Marsden PK, Cook G Jr. Dissociation between global markers of bone formation and direct measurement of spinal bone formation in osteoporosis. *J Bone Miner Res.* 2004;19:1797–1804.
32. Puri T, Blake GM, Frost ML, et al. Comparison of six quantitative methods for the measurement of bone turnover at the hip and lumbar spine using ^{18}F-fluoride PET-CT. *Nucl Med Commun.* 2012;33:597–606.
33. Cook GJ, Lodge MA, Marsden PK, Dynes A, Fogelman I. Non-invasive assessment of skeletal kinetics using fluorine-18 fluoride positron emission tomography:

evaluation of image and population-derived arterial input functions. *Eur J Nucl Med.* 1999;26:1424–1429.
34. Blake GM, Siddique M, Puri T, et al. A semipopulation input function for quantifying static and dynamic ^{18}F-fluoride PET scans. *Nucl Med Commun.* 2012;33:881–888.
35. Brenner W, Vernon C, Muzi M, et al. Comparison of different quantitative approaches to ^{18}F-fluoride PET scans. *J Nucl Med.* 2004;45:1493–1500.
36. Nadel HR. Bone scan update. *Semin Nucl Med.* 2007;37:332–339.
37. Sharma P, Kumar R, Singh H, et al. Indeterminate lesions on planar bone scintigraphy in lung cancer patients: SPECT, CT or SPECT-CT? *Skeletal Radiol.* 2012;41:843–850.
38. Buyukdereli G, Guney IB, Ozerdem G, Kesiktas E. Evaluation of vascularized graft reconstruction of the mandible with Tc-99m MDP bone scintigraphy. *Ann Nucl Med.* 2006;20:89–93.
39. Hervás I, Floria LM, Bello P, et al. Microvascularized fibular graft for mandibular reconstruction: detection of viability by bone scintigraphy and SPECT. *Clin Nucl Med.* 2001;26:225–229.
40. Kirschner MH, Manthey N, Tatsch K, Nerlich A, Hahn K, Hofmann GO. Use of three-phase bone scans and SPET in the follow-up of patients with allogenic vascularized femur transplants. *Nucl Med Commun.* 1999;20:517–524.
41. Lauer I, Czech N, Zieron J, Sieg P, Richter E, Baehre M. Assessment of the viability of microvascularized bone grafts after mandibular reconstruction by means of bone SPET and semiquantitative analysis. *Eur J Nucl Med.* 2000;27:1552–1556.
42. Rojvachiranonda N, Tepmongkol S, Mahatumarat C. Quantitative study of new bone formation in distraction osteogenesis of craniofacial bones by bone scintigraphy. *J Craniofac Surg.* 2007;18:1236–1241.
43. Brenner W, Vernon C, Conrad EU, Eary JF. Assessment of the metabolic activity of bone grafts with ^{18}F-fluoride PET. *Eur J Nucl Med Mol Imaging.* 2004;31:1291–1298.
44. Schliephake H, Berding G, Knapp WH, Sewilam S. Monitoring of graft perfusion and osteoblast activity in revascularised fibula segments using [^{18}F]-positron emission tomography. *Int J Oral Maxillofac Surg.* 1999;28:349–355.
45. Berding G, Schliephake H, van den Hoff J, Knapp WH. Assessment of the incorporation of revascularized fibula grafts used for mandibular reconstruction with F-18-PET. *Nuklearmedizin.* 2001;40:51–58.
46. Goldberg VM. Selection of bone grafts for revision total hip arthroplasty. *Clin Orthop Relat Res.* 2000;68–76.
47. Piert M, Winter E, Becker GA, et al. Allogenic bone graft viability after hip revision arthroplasty assessed by dynamic [^{18}F]fluoride ion positron emission tomography. *Eur J Nucl Med.* 1999;26:615–624.
48. Temmerman OP, Raijmakers PG, Heyligers IC, et al. Bone metabolism after total hip revision surgery with impacted grafting: evaluation using H2 ^{15}O and [^{18}F] fluoride PET: a pilot study. *Mol Imaging Biol.* 2008;10:288–293.
49. Sörensen J, Ullmark G, Langstrom B, Nilsson O. Rapid bone and blood flow formation in impacted morselized allografts: positron emission tomography (PET) studies on allografts in 5 femoral component revisions of total hip arthroplasty. *Acta Orthop Scand.* 2003;74:633–643.
50. Heyligers IC, Klein-Nulend J. Detection of living cells in non-processed but deep-frozen bone allografts. *Cell Tissue Bank.* 2005;6:25–31.
51. Dasa V, Adbel-Nabi H, Anders MJ, Mihalko WM. F-18 fluoride positron emission tomography of the hip for osteonecrosis. *Clin Orthop Relat Res.* 2008;466:1081–1086.
52. Schiepers C, Broos P, Miserez M, Bormans G, De Roo M. Measurement of skeletal flow with positron emission tomography and ^{18}F-fluoride in femoral head osteonecrosis. *Arch Orthop Trauma Surg.* 1998;118:131–135.
53. Ullmark G, Sundgren K, Milbrink J, Nilsson O, Sorensen J. Metabolic development of necrotic bone in the femoral head following resurfacing arthroplasty: a clinical [^{18}F]fluoride-PET study in 11 asymptomatic hips. *Acta Orthop.* 2012;83:22–25.
54. Loberg RD, Logothetis CJ, Keller ET, Pienta KJ. Pathogenesis and treatment of prostate cancer bone metastases: targeting the lethal phenotype. *J Clin Oncol.* 2005;23:8232–8241.
55. Patel LR, Camacho DF, Shiozawa Y, Pienta KJ, Taichman RS. Mechanisms of cancer cell metastasis to the bone: a multistep process. *Future Oncol.* 2011;7:1285–1297.
56. Chang MC, Chen JH, Liang JA, et al. Meta-analysis: comparison of F-18 fluorodeoxyglucose-positron emission tomography and bone scintigraphy in the detection of bone metastasis in patients with lung cancer. *Acad Radiol.* 2012;19:349–357.
57. Kawaguchi M, Tateishi U, Shizukuishi K, Suzuki A, Inoue T. ^{18}F-fluoride uptake in bone metastasis: morphologic and metabolic analysis on integrated PET/CT. *Ann Nucl Med.* 2010;24:241–247.
58. Bortot DC, Amorim BJ, Oki GC, et al. ^{18}F-fluoride PET/CT is highly effective for excluding bone metastases even in patients with equivocal bone scintigraphy. *Eur J Nucl Med Mol Imaging.* 2012;39:1730–1736.
59. Krüger S, Buck AK, Mottaghy FM, et al. Detection of bone metastases in patients with lung cancer: ^{99m}Tc-MDP planar bone scintigraphy, ^{18}F-fluoride PET or ^{18}F-FDG PET/CT. *Eur J Nucl Med Mol Imaging.* 2009;36:1807–1812.
60. Jadvar H, Desai B, Ji L, et al. Prospective evaluation of ^{18}F-NaF and ^{18}F-FDG PET/CT in detection of occult metastatic disease in biochemical recurrence of prostate cancer. *Clin Nucl Med.* 2012;37:637–643.
61. Beheshti M, Vali R, Waldenberger P, et al. Detection of bone metastases in patients with prostate cancer by ^{18}F fluorocholine and ^{18}F fluoride PET-CT: a comparative study. *Eur J Nucl Med Mol Imaging.* 2008;35:1766–1774.
62. Fizazi K, Albiges L, Massard C, Escudier B, Loriot Y. Novel and bone-targeted agents for CRPC. *Ann Oncol.* 2012;23(suppl 10):x264–x267.
63. Dennis ER, Jia X, Mezheritskiy IS, et al. Bone scan index: a quantitative treatment response biomarker for castration-resistant metastatic prostate cancer. *J Clin Oncol.* 2012;30:519–524.
64. Brown MS, Chu GH, Kim HJ, et al. Computer-aided quantitative bone scan assessment of prostate cancer treatment response. *Nucl Med Commun.* 2012;33:384–394.
65. Smith DC, Smith MR, Sweeney C, et al. Cabozantinib in patients with advanced prostate cancer: results of a phase II randomized discontinuation trial. *J Clin Oncol.* 2013;31:412–419.
66. Doot RK, Muzi M, Peterson LM, et al. Kinetic analysis of ^{18}F-fluoride PET images of breast cancer bone metastases. *J Nucl Med.* 2010;51:521–527.
67. Cook GJ, Parker C, Chua S, Johnson B, Aksnes AK, Lewington VJ. ^{18}F-fluoride PET: changes in uptake as a method to assess response in bone metastases from castrate-resistant prostate cancer patients treated with ^{223}Ra-chloride (Alpharadin). *EJNMMI Res* 2011;1:4.
68. Griffith K, Pearson D, Parker C, Thorpe S, Vincent RM, Hosking DJ. The use of a whole body index with bone scintigraphy to monitor the response to therapy in Paget's disease. *Nucl Med Commun.* 2001;22:1069–1075.
69. Rubini G, Lauriero F, Rubini D, D'Addabbo A. 99Tcm-MDP global skeletal uptake and markers of bone metabolism in patients with bone diseases. *Nucl Med Commun.* 1993;14:567–572.
70. Israel O, Front D, Hardoff R, Ish-Shalom S, Jerushalmi J, Kolodny GM. In vivo SPECT quantitation of bone metabolism in hyperparathyroidism and thyrotoxicosis. *J Nucl Med.* 1991;32:1157–1161.
71. Cook GJ, Blake GM, Marsden PK, Cronin B, Fogelman I. Quantification of skeletal kinetic indices in Paget's disease using dynamic ^{18}F-fluoride positron emission tomography. *J Bone Miner Res.* 2002;17:854–859.
72. Waterval JJ, Van Dongen TM, Stokroos RJ, et al. Bone metabolic activity in hyperostosis cranialis interna measured with ^{18}F-fluoride PET. *Eur J Nucl Med Mol Imaging.* 2011;38:884–893.
73. Piert M, Machulla HJ, Jahn M, Stahlschmidt A, Becker GA, Zittel TT. Coupling of porcine bone blood flow and metabolism in high-turnover bone disease measured by [^{15}O]H_2O and [^{18}F]fluoride ion positron emission tomography. *Eur J Nucl Med Mol Imaging.* 2002;29:907–914.
74. Piert M, Zittel TT, Jahn M, Stahlschmidt A, Becker GA, Machulla HJ. Increased sensitivity in detection of a porcine high-turnover osteopenia after total gastrectomy by dynamic ^{18}F-fluoride ion PET and quantitative CT. *J Nucl Med.* 2003;44:117–124.
75. Schiepers C, Nuyts J, Bormans G, et al. Fluoride kinetics of the axial skeleton measured in vivo with fluorine-18-fluoride PET. *J Nucl Med.* 1997;38:1970–1976.
76. Kurata S, Shizukuishi K, Tateishi U, et al. Age-related changes in pre- and postmenopausal women investigated with ^{18}F-fluoride PET: a preliminary study. *Skeletal Radiol.* 2012;41:947–953.
77. de Nijs RN, Jacobs JW, Lems WF, et al. Alendronate or alfacalcidol in glucocorticoid-induced osteoporosis. *N Engl J Med.* 2006;355:675–684.
78. Peris P, Alvarez L, Vidal S, Martinez MA, Monegal A, Guanabens N. Treatment with tiludronate has a similar effect to risedronate on Paget's disease activity assessed by bone markers and bone scintigraphy. *Clin Exp Rheumatol.* 2007;25:206–210.
79. Installé J, Nzeusseu A, Bol A, Depresseux G, Devogelaer JP, Lonneux M. ^{18}F-fluoride PET for monitoring therapeutic response in Paget's disease of bone. *J Nucl Med.* 2005;46:1650–1658.
80. Uchida K, Nakajima H, Miyazaki T, et al. Effects of alendronate on bone metabolism in glucocorticoid-induced osteoporosis measured by ^{18}F-fluoride PET: a prospective study. *J Nucl Med.* 2009;50:1808–1814.

The Journal of NUCLEAR MEDICINE

Dynamic Bone Imaging with ^{99m}Tc-Labeled Diphosphonates and ^{18}F-NaF: Mechanisms and Applications

Ka Kit Wong and Morand Piert

J Nucl Med. 2013;54:590-599.
Published online: March 12, 2013.
Doi: 10.2967/jnumed.112.114298

The Journal of Nuclear Medicine is published monthly.
SNMMI | Society of Nuclear Medicine and Molecular Imaging
1850 Samuel Morse Drive, Reston, VA 20190.
(Print ISSN: 0161-5505, Online ISSN: 2159-662X)

SNMMI SOCIETY OF NUCLEAR MEDICINE AND MOLECULAR IMAGING